Distribution of cardiac sodium channels in clusters potentiates ephaptic interactions in the intercalated disc

Echrak Hichri[1], Hugues Abriel[2] and Jan P. Kucera[1]

[1] Department of Physiology, University of Bern, Bern, Switzerland

[2] Institute of Biochemistry and Molecular Medicine, University of Bern, Bern, Switzerland

Running title: Ephaptic effects in intercalated discs

Keywords: ephaptic transmission; cardiac sodium current; cardiac action potential; patch clamp experiments; computer simulations

Corresponding author:

Jan P. Kucera

Department of Physiology, University of Bern, Bühlplatz 5, 3012 Bern, Switzerland

E-mail: kucera@pyl.unibe.ch

Table of Contents category: Cardiovascular

Key points summary

- It was proposed that ephaptic interactions mediated by extracellular potentials might contribute to cardiac conduction when gap junctional coupling is reduced, but this mechanism is still controversial.

- In intercalated discs, sodium (Na^+) channels form clusters near gap junction plaques, but the functional significance of these clusters was never evaluated.

- In experiments with HEK cells expressing cardiac Na^+ channels, we show that restricting the extracellular space modulates the Na^+ current as predicted by corresponding simulations accounting for ephaptic effects.

- In a high-resolution model of the intercalated disc, ephaptic impulse transmission from one cell to another is facilitated by clusters of Na^+ channels facing each other across the intercellular cleft when gap junctional coupling is reduced.

- Thus, our simulations reveal a functional role for the clustering of Na^+ channels in intercalated discs, suggesting that conditions leading to their rearrangement may have repercussions on cardiac conduction.

Abstract

It has been proposed that ephaptic interactions in intercalated discs, mediated by extracellular potentials, contribute to cardiac impulse propagation when gap junctional coupling is reduced. However, experiments demonstrating ephaptic effects on the cardiac Na^+ current (I_{Na}) are scarce. Furthermore, Na^+ channels form clusters in perinexal regions, but the electrophysiological significance of this clustering has never been investigated. In patch clamp experiments with HEK cells stably expressing human $Na_v1.5$ channels, we examined how I_{Na} elicited by an activation protocol is modulated by restricting the extracellular space. Using a high-resolution model of the intercalated disc, we then investigated how the distribution of Na^+ channels influences ephaptic interactions. In the experiments, approaching the cell to a non-conducting obstacle always increased peak I_{Na} at step potentials near the threshold of I_{Na} activation and decreased peak I_{Na} at step potentials far above threshold (7 cells, p=0.0156, Wilcoxon signed rank test). These effects were consistent with corresponding simulations accounting for ephaptic interactions. In the intercalated disc model, ephaptic effects were potentiated by redistributing the Na^+ channels into a central cluster of the disc. Moreover, ephaptic impulse transmission from one cell to another was facilitated by clusters of Na^+ channels facing each other across the intercellular cleft when gap junctional coupling was reduced. In conclusion, our proof-of-principle experiments demonstrate that cardiac I_{Na} is modulated by a confinement of extracellular space, and our simulations reveal the functional role of the aggregation of Na^+ channels in the perinexus. These findings highlight novel concepts in the physiology of cardiac excitation.

Abbreviations. I_{Na}: sodium current; V_e extracellular potential; AP, action potential.

Introduction

Action potential (AP) propagation is essential for the proper function of the heart. Disturbances of cardiac AP propagation (slow conduction, conduction block) can lead to arrhythmias (Kléber & Rudy 2004). It is widely accepted that cardiac AP propagation occurs via depolarizing electrotonic current flow through gap junctions (Weidmann 1970; Kléber & Rudy 2004). Under physiological conditions, the current that underlies the rapid upstroke of the cardiac AP is the Na^+ current carried by voltage-gated $Na_v1.5$ channels. This current provides the charge necessary to depolarize downstream tissue (Kléber & Rudy 2004). The Na^+ current (I_{Na}) and the level of gap junctional coupling are thus the principal determinants of cardiac conduction (Shaw & Rudy 1997; Kléber & Rudy 2004). Gap junction channels are expressed at high density in intercalated discs, thereby ensuring rapid conduction along myocardial fibres (Dolber *et al.* 1992). Intriguingly, Na^+ channels are also expressed at high density in intercalated discs (Cohen 1996; Maier *et al.* 2002; Lin *et al.* 2011; Shy *et al.* 2013; Leo-Macias *et al.* 2016), where, according to most recent estimations, about 50% of Na^+ channels are located (Lin *et al.* 2011; Shy *et al.* 2013; Leo-Macias *et al.* 2016). A high density of Na^+ channels was also observed at intercellular contacts in cardiomyocyte cultures (Kucera *et al.* 2002).

This high density of Na^+ channels in intercalated discs suggests the involvement of an alternate conduction mechanism, called "electric field mechanism" (Sperelakis & Mann 1977; Sperelakis 2002), "ephaptic conduction" (Mori *et al.* 2008) or "ephaptic coupling" (Lin & Keener 2010). Ephaptic coupling relies on the large number of Na^+ channels in the membranes adjacent to the restricted intercellular cleft of the intercalated disc. According to this mechanism, upon activation of the Na^+ channels in the membrane on one side of the intercalated disc, the large Na^+ current flowing radially through the large resistance of the narrow extracellular space causes (according to Ohm's law) a substantial negative extracellular potential (V_e) within the cleft. This negative V_e then translates into membrane depolarization on the other side of the cleft, where it contributes to the activation of Na^+ channels and thus to cardiac conduction (Veeraraghavan *et al.* 2014), in conjunction or in interaction with the classical mechanism based on electrotonic current flow through gap junctions (Weidmann 1970).

It was recently reported that in intercalated discs, Na^+ channels are localized in the vicinity of gap junctional plaques (Rhett & Gourdie 2012; Rhett *et al.* 2013; Veeraraghavan *et al.* 2014). This finding has led to the concept of "perinexus", a region where connexin 43 (the principal gap junction channel forming protein in ventricular myocardium) and Na^+ channels interact with structural and regulatory proteins, highlighting a potential role of the perinexus in cardiac electrical function (Rhett & Gourdie 2012; Rhett *et al.* 2013; Vermij *et al.* 2017). A clustering of Na^+ channels in intercalated discs was also reported in further morphological studies (Leo-Macias *et al.* 2016).

The ephaptic coupling mechanism is still controversial, even decades after it has been proposed. This controversy is certainly related to the fact that a direct characterization of this mechanism is extremely difficult experimentally and that a clear direct experimental proof at the cellular level is still absent. For this reason, ephaptic conduction was essentially studied in mathematical models (Sperelakis & Mann 1977; Kucera *et al.* 2002; Mori *et al.* 2008; Lin & Keener 2010; Tsumoto *et al.* 2011; Wei *et al.* 2016). These studies have shown that ephaptic coupling can indeed contribute to action potential propagation when the level of gap junctional coupling is reduced or even absent. These mathematical models also explain paradoxical effects of Na^+ channel blockers, of gap junctional uncouplers and of changes in extracellular Na^+ and K^+ concentrations on conduction velocity and its anisotropy ratio in optical mapping studies of whole hearts (George *et al.* 2015; Veeraraghavan *et al.* 2015). These effects cannot be explained based on gap junctional coupling alone, thus providing support for the involvement of ephaptic coupling. Moreover, in connexin 43 knockout cardiac tissue, it was observed that the resulting slowing of conduction was smaller than expected from theories and models built upon electrotonic gap junctional coupling (Gutstein *et al.* 2001; Beauchamp *et al.* 2004; van Rijen *et al.* 2004), again indirectly suggesting a potential involvement of ephaptic coupling in conduction. However, all these modelling studies considered a uniform distribution of Na^+ channels at intercellular junctions and the electrophysiological significance of the reported Na^+ channel clustering was never examined.

In this work, our first aim was to provide experimental evidence at the cellular level that ephaptic effects modulate I_{Na} via V_e when the extracellular space is restricted by bringing the cell in proximity to a non-conductive obstacle. Using cells expressing human $Na_v1.5$

channels, we show that restricting the extracellular space near the cell modulates I_{Na}. The modulation of I_{Na} was consistent with computer simulations using a new high-resolution model of excitable membranes facing a narrow extracellular cleft that we developed using the finite element method. Using this model, our second aim was to evaluate the effects of Na^+ channel distribution on ephaptic interactions and its consequences on ephaptic transmission. We found that aggregating Na^+ channels together potentiates ephaptic phenomena and AP transmission from one cell to the other, in particular when clusters of Na^+ channels face each other across the intercellular cleft. These effects are due to complex spatiotemporal interactions between I_{Na} and V_e that were revealed thanks to our high-resolution modelling studies.

Methods

Patch clamp experiments

Human embryonic kidney 293 (HEK293) cells stably expressing wild-type human cardiac $Na_v1.5$ channels were prepared and cultured at a low seeding density as described previously (Dhar Malhotra *et al.* 2001). The Na^+ current (I_{Na}) was recorded using the patch clamp technique in the whole cell configuration at room temperature (22 °C) with glass pipettes of 1.9-2.6 MΩ resistance using a standard amplifier (Axopatch200B, Molecular Devices Corp., Sunnyvale CA, USA). Experiments were controlled using the pClamp10 software (Molecular Devices Corp., Sunnyvale CA, USA). Pipette capacitance and series resistance were compensated to 80–85 %. The Na^+ current was low pass filtered (cut-off frequency: 4 kHz) and recorded digitally at a sampling rate of 20 kHz. Residual capacitive transients and time-independent leak currents were subtracted using a P/4 protocol. The cells were bathed in a medium containing (mmol/L): NaCl 10, N-methyl-D-glutamine-Cl 80, $CaCl_2$ 2, $MgCl_2$ 1.2, CsCl 5, HEPES 10, and Glucose 5, adjusted to a pH of 7.40 using 3 mol/L CsOH. The pipettes were filled with an intracellular solution composed of (mmol/L): Na_2-ATP 5, Cs aspartate 70, CsCl 60, EGTA 11, HEPES 10, $CaCl_2$ 1, and $MgCl_2$ 1, adjusted to a pH of 7.20 using HCl. The amplifier head stage was mounted on a high-precision motorized micromanipulator (MP-225, Sutter Instrument,

Novato, CA, USA). The liquid junction potential (estimated to be 21.5 mV) was not compensated.

A steady-state activation protocol was used to examine peak I_{Na} and to establish steady-state activation current-voltage relationships. It consisted of 30 ms long voltage steps to –90 to +30 mV in increments of 5 mV, separated by 3 s intervals at the holding potential of –90 mV.

Restricting the extracellular space

Every cell was first subjected to a steady-state activation (current-voltage, IV) protocol. The cell was then detached from the growth substrate without losing the gigaohm seal by applying a gentle pipette movement in the horizontal directions using the motorized micromanipulator. The steady state activation protocol was repeated with the cell then assuming a spherical shape. Subsequently, in order to restrict the extracellular space near a region of the cell membrane, the cell was approached slowly to a non-conducting obstacle consisting of a molten glass pipette tip having a spherical shape with a radius of approx. 100 µm. The cell was moved under visual control using phase contrast microscopy and video monitoring in a focal plane perpendicular to the glass obstacle and passing through the cell. The cell was approached gently to the obstacle until a slight deformation of the cell was observed, confirming close physical contact. The steady-state activation protocol was then repeated. Finally, the cell was moved away (>10 µm from the obstacle), and the steady-state activation protocol was repeated one last time.

Data Analysis

The currents were analysed using the Clampfit software (Molecular Devices Corp., Sunnyvale CA, USA) and custom-written programs in MATLAB (The Math Works, Natick, MA).

The currents were normalized by cell capacitance and filtered using a 5-sample moving average filter. Then, peak currents were fitted to a Boltzmann function, $f(V_m)=1/(1+\exp((V_m-V_{1/2})/K)))$, where f is the normalized current or conductance, V_m is

the membrane potential, $V_{1/2}$ is the voltage at which half of the available channels are activated, and K is the slope factor.

Computer model

Mathematical model of excitable membranes with a restricted extracellular space

The interactions between I_{Na} and the extracellular potential (V_e) were investigated using high-resolution two-dimensional models of membranes adjacent to a narrow extracellular space. Two situations were investigated. In the first situation, we modelled one cell membrane facing a non-conductive obstacle and separated from it by a narrow cleft. This corresponds to the experiments described above. In the second situation, we modelled two cell membranes separated by a narrow intercellular cleft. This situation corresponds to the membranes of two longitudinally abutting cardiomyocytes separated by an intercalated disc.

For the first situation, charge conservation in the membrane-cleft system was described by

$$-\nabla(w\sigma_e\nabla V_e) = i_{ion} + c\frac{dV_m}{dt}, \tag{Eq. 1}$$

where w is the cleft width, σ_e is the extracellular conductivity tensor, i_{ion} is the ion current density through the membrane, c is the specific membrane capacitance (1 µF/cm^2) and V_m is the transmembrane potential ($V_m = V_i - V_e$). The left hand side of Eq. 1 represents a Laplacian term in the two dimensions of the membrane. Because cleft width is considerably smaller than the spatial extent of the membrane, it was assumed that gradients of V_e in the direction perpendicular to the membrane are negligible. The extracellular space was considered isotropic and σ_e was set to a scalar value of 6.667 mS/cm (resistivity: 150 Ωcm).

For the second situation, charge conservation was described by

$$-\nabla(w\sigma_e\nabla V_e) = i_{ion,1} + c\frac{dV_{m,1}}{dt} + i_{ion,2} + c\frac{dV_{m,2}}{dt}, \tag{Eq. 2}$$

where, $i_{ion,1}$ and $i_{ion,2}$ are the ion current densities through the two membranes, and $V_{m,1}$ and $V_{m,2}$ are the respective transmembrane potentials.

The ionic current density was formulated as

$$i_{ion} = i_{Na} + i_K, \qquad\qquad\qquad \text{(Eq. 3)}$$

where i_{Na} is the Na^+ current density and i_K represents all other ion currents. The Na^+ current density was represented using a Hodgkin-Huxley formalism according to Luo and Rudy (Luo & Rudy 1991, 1994) with modifications proposed by Livshitz and Rudy (Livshitz & Rudy 2009) as

$$i_{Na} = g_{Na} \cdot m^3 hj \cdot (V_m - E_{Na}), \qquad\qquad \text{(Eq. 4)}$$

with g_{Na} being the maximum conductance per unit area (23 mS/cm^2 (Luo & Rudy 1991)), m the activation gating variable, h and j the inactivation gating variables, and E_{Na} the Nernst potential for Na^+. E_{Na} was set to +55 mV.

Because our principal goal was to study the interactions between V_e and I_{Na}, which last only a few milliseconds, we did not implement the detail of other time-dependent ionic currents or calcium-induced calcium release, and lumped all the other currents into one single repolarizing linear K^+ current as

$$i_K = g_K \cdot (V_m - E_K), \qquad\qquad\qquad \text{(Eq. 5)}$$

with $g_K = 0.3$ mS/cm^2 and $E_K = -85$ mV. This formulation sets the resting membrane potential at E_K.

As previously shown, the density of Na^+ channels is higher in intercalated discs than on the lateral membranes (Cohen 1996; Maier *et al.* 2002; Leo-Macias *et al.* 2016). The current consensus is that a proportion P of approximately 50% of the whole cell Na^+ current is present in the intercalated disc membranes (Lin *et al.* 2011; Shy *et al.* 2013; Leo-Macias *et al.* 2016). Compared to a uniform distribution over the entire cell surface, g_{Na} is therefore scaled (increased) in the disc membrane by a factor Fg_{Na} defined as

$$F_{g_{Na}} = P \frac{A_{cell}}{A_{discs}},$$ (Eq. 6)

with A_{cell} being the area of the cell and A_{discs} the area of the membranes adjacent to intercalated discs. This factor was incorporated as a multiplier into Eq. 4. For a cylindrical cardiac cell with typical length L=100 µm and radius r=11 µm, this scaling factor is 5.05 for P=50% and would be 10.09 for P=100% in the extreme case of all channels being located in the intercalated discs. Therefore, in the simulations, g_{Na} was scaled by various factors ranging from 1 to 10.09.

Morphological studies have also shown that Na^+ channels form clusters in intercalated discs (Rhett *et al.* 2013; Veeraraghavan *et al.* 2015; Leo-Macias *et al.* 2016). The specific effect of Na^+ channel clustering was investigated in dedicated simulations in which g_{Na} was redistributed into selected membrane regions while keeping constant the total Na^+ current conductance (the integral of g_{Na} over the entire membrane).

Numerical methods

Unless specified otherwise, the membranes were modelled as discs with a predefined radius. The model described by partial differential Eqs. 1 and 2 was discretized using triangular finite elements with piecewise linear basis functions (Johnson 1987; Sundnes *et al.* 2006). Meshes were generated in MATLAB using the function "generateMesh". The maximal edge length was set to 0.05 times the disc radius. From the finite elements, Eq. 1 was approximated by a system of ordinary differential equations,

$$\mathbf{K}v_e = \mathbf{M} \frac{dv_m}{dt} + F_{i_{ion}},$$ (Eq. 7)

Where V_e is the vector of the V_e's at the mesh vertices, $\mathbf{K}$ is the conductance matrix for the extracellular space (stiffness matrix), $\mathbf{M}$ is the capacitance matrix (mass matrix) computed using c, and Fi_{ion} is the vector of ion currents at the vertices (load vector). We simulated voltage clamp protocols controlling V_i (or $V_{i,1}$ and $V_{i,2}$). During a voltage step, dV_m/dt in Eq. 7 is therefore equal to $-dV_e/dt$. Because the intracellular space is not confined and has a low resistance compared to the cleft, V_i was assumed to be spatially uniform.

Similarly, Eq. 2 was discretized as

$$\mathbf{K}v_e = \mathbf{M_1}\frac{dv_{m,1}}{dt} + F_{i_{ion,1}} + \mathbf{M_2}\frac{dv_{m,2}}{dt} + F_{i_{ion,2}}, \qquad\qquad \text{(Eq. 8)}$$

in which $\mathbf{M_1}=\mathbf{M_2}=\mathbf{M}$ if the two membranes have the same shape and specific capacitance. Assuming that extracellular gradients and potentials are negligible in the bulk extracellular space (outside the cleft), the systems described by Eqs. 7 and 8 were subjected to a Dirichlet boundary condition $V_e=0$ at the rim of the disc, where the narrow cleft space joins the extended bulk space. Another Dirichlet boundary condition was applied on the intracellular potentials (V_i, or $V_{i,1}$ and $V_{i,2}$) by enforcing the predefined voltage clamp protocols. These protocols consisted of depolarizing steps starting at a holding potential of –85 mV (resting potential). As initial condition, V_e was set to 0 in the entire cleft space and the gating variables m, h, and j were set to their corresponding steady-state values.

Eqs. 7 and 8 were integrated using an operator splitting method (Sundnes *et al.* 2006) with a constant time step Δt of 0.05 µs. The diffusive part of the system was integrated using the Crank-Nicolson method (Crank & Nicholson 1947) by solving the following system at each time step:

$$\left(\bar{\mathbf{M}} - \tfrac{1}{2}\bar{\mathbf{K}}\Delta t\right)v_e(t + \Delta t) = \left(\bar{\mathbf{M}} + \tfrac{1}{2}\bar{\mathbf{K}}\Delta t\right)v_e(t), \qquad\qquad \text{(Eq. 9)}$$

where $\bar{\mathbf{M}}$ and $\bar{\mathbf{K}}$ are reduced matrices obtained from $\mathbf{M}$ and $\mathbf{K}$ (or $\mathbf{M_1}$, $\mathbf{M_2}$ and $\mathbf{K}$) after having enforced the Dirichlet conditions and v_e is the vector of the unknown V_e's at the mesh vertices. Taking advantage from the fact that the left hand side operator in Eq. 8 is a sparse symmetric matrix, the system was solved using the Cholesky decomposition of this matrix, which needed to be computed only once at the beginning of each simulation. The gating variables were integrated using the method of Rush and Larsen (Rush & Larsen 1978).

To obtain macroscopic Na$^+$ currents, the Na$^+$ current density was integrated over the entire disc membrane. Reference simulations without feedback of V_e on I_{Na} were run by maintaining $V_e=0$ in the entire cleft.

Statistics

For experimental results, significance was assessed at the 0.05 level using the 2-tailed Wilcoxon signed rank test (non-normal data distribution).

Results

Restricting the extracellular space has a dual activating and attenuating effect on I_{Na} with complex spatiotemporal dynamics

To understand the behaviour of I_{Na} and its interaction with V_e in patch clamp experiments with cells expressing Na^+ channels brought in proximity to a non-conductive obstacle, we first conducted corresponding simulations of a disc-shaped membrane with a uniform distribution of channels adjacent to a narrow extracellular space. Figure 1A illustrates the model circuit equivalent and the finite element mesh. The factor F_{gNa} was set to 10.09, which, based on typical cell geometries in vivo, corresponds to the situation in which all channels are located at the extremity of the myocytes. The intracellular side of the membrane was subjected to a voltage clamp activation protocol. Figure 1B illustrates the spatiotemporal behaviour of I_{Na}, V_e, the activation gate *m* and the product of the inactivation gates *hj* for various cleft widths, for a step to –25 mV (far above the I_{Na} activation threshold) and –50 mV (near the threshold).

At $V_{step} = –25$ mV, the presence of a restricted cleft decreased the peak of total I_{Na}. This effect increased with decreasing cleft width. The I_{Na} decrease was due to the diminished driving force (V_m–E_{Na}) resulting from the negative V_e in the cleft. In turn, this negative V_e was the consequence of the current flowing radially through the extracellular space. As shown in the corresponding colour plots and in Figure 1C, V_e was not spatially homogeneous but exhibited a radially symmetric concave profile, with a minimum in the cleft centre. Thus, the feedback of V_e on I_{Na} dynamics was stronger in the centre of the disc. The colour plots for $V_{step} = –25$ mV and a 20 nm wide cleft and Movie 1 show that a substantially negative V_e appeared first in the centre of the disc. There, the strongly negative V_e (and thus the more positive V_m) precipitated I_{Na} inactivation. Because of the spatially heterogeneous behaviour of V_e and inactivation (product *hj*), the local density of

I_{Na} was also heterogeneous: local I_{Na} was maximal (in absolute value) and lasted longer in the periphery of the disc, and the self-attenuation of I_{Na} was stronger in the centre.

At $V_{step} = -50$ mV, total I_{Na} was small in the absence of a cleft but strongly potentiated for cleft widths from 10 to 80 nm. For a 20 nm wide cleft, as shown in the colour plots and in Movie 2, the negative V_e building up in the centre supported there the activation of I_{Na} (gate *m*), whereas *m* remained low in the periphery. In a positive feedback, the increasing I_{Na} in the centre rendered V_e even more negative, until, in turn, inactivation was precipitated. In conjunction with the decreased driving force, I_{Na} in the centre was small and short lasting. In contrast, in the periphery, the driving force was reduced to a lesser extent and inactivation was not accelerated. As a result, I_{Na} was activated later but was more intense and lasted longer near the periphery of the disc. Thus, globally, the presence of a narrow cleft accelerated and increased I_{Na} in a self-activating feedback mechanism. However, the self-attenuating mechanism was still present. Consequently, peak total I_{Na} exhibited a biphasic behaviour with decreasing left width, and, for very narrow clefts, peak I_{Na} became smaller because of increasing self-attenuation. Thus, the dynamics were different at $V_{step} = -25$ mV and $V_{step} = -50$ mV. At -25 mV, decreasing cleft width caused a monotonic decrease of peak total I_{Na}, whereas at -50 mV, decreasing cleft width first caused an increase, followed by a decrease.

These dynamics can be further understood by examining the minimum of V_e as a function of cleft width (Figure 1D). At $V_{step} = -25$ mV, minimal V_e decreased progressively with cleft width. However, at $V_{step} = -50$ mV, V_e remained in the range of only a few mV for cleft widths ≥ 90 nm, and became abruptly negative only when cleft width was <80 nm (arrow in Figure 1D). This abrupt behaviour is explained by the fact that the self-activating positive feedback mechanism described above appears only with sufficiently narrow clefts.

Figure 1E shows the relationships between peak total I_{Na} and V_{step} (IV curves) for various cleft widths and corresponding steady state activation curves reconstructed using the same analysis as in patch clamp studies. When total I_{Na} was considered, the self-attenuating mechanism described above caused peak I_{Na} to be smaller (in absolute value) for potentials ≥ 20 mV more positive than the midpoint of activation of the control IV curve without cleft. Narrowing the cleft thus lowered and accentuated the threshold behaviour of I_{Na}. Conversely, for potentials ≥ 10 mV more negative than this midpoint,

peak I_{Na} was larger due to self-activation. In terms of steady state activation curves, the presence of a cleft caused a shift to more negative potentials and a steepening of the voltage-dependence of activation.

Ephaptic effects are modulated by cleft width and size, cleft geometry and the density of Na⁺ channels

In intact myocardium, myocyte width and thus intercalated disc size is variable between species and between individual cells, and it can be affected by disease (e.g., hypertrophy). Moreover, the expression of Na⁺ channels within the disc and the proportion of Na⁺ channels located in disc membranes may also exhibit an intercellular variability. In the patch clamp experiments that we conducted, the size of the contact with the unexcitable obstacle and the Na⁺ channel expression in the HEK cells is variable as well. Therefore, we explored the effects of varying the cleft size and geometry and the Na⁺ channel density in the membrane facing the restricted extracellular space while keeping the Na⁺ channel distribution uniform. We conducted simulations with the same model as in the previous section and varied the radius of the disc-shaped membrane, the Na⁺ channel density (by varying F_{gNa}) and the width of the cleft. In addition, we investigated the effect of changing the shape of the cleft from a disc to an elongated ellipse. This geometry mimics that of intercellular contacts in monolayer cultures of cardiomyocytes, where the length of the contact is several fold larger than the thickness of the cultured cells (Jousset *et al.* 2016). Figure 2A represents normalized peak total I_{Na} during an activation step from –85 to –25 mV (top) and –50 mV (bottom) as a function of cleft width for different F_{gNa} (1, 5.05 and 10.09, columns in Figure 2A). In each plot, normalized peak I_{Na} is represented for various disc-shaped cleft radii (11, 7, 5.5 and 2.75 µm) as well as for an ellipse-shaped cleft (semi-major axis: 11 µm; semi-minor axis: 2.75 µm). Peak I_{Na} was normalized to peak I_{Na} in the absence of a cleft. Values <1 signify that peak I_{Na} is smaller in absolute value and thus imply self-attenuation, while values >1 imply self-activation.

At V_{step} = –25 mV, for F_{gNa} = 1, normalized peak I_{Na} was close to or just below 1 for all cleft geometries and all cleft widths, indicating that peak I_{Na} was comparable to peak I_{Na} in the absence of a cleft. However, when F_{gNa} was increased to 5.05, normalized peak I_{Na} decreased <1 for narrow cleft widths and reached smaller values as disc radius was

increased. For the elliptic disc, the behaviour of normalized peak I_{Na} was similar to that for the disc-shaped cleft with a radius of 2.75 µm. When F_{gNa} was further increased to 10.09, these observations were accentuated. These results indicate that increasing Na^+ channel density leads to decreasing peak I_{Na} and thus to stronger self-attenuation, in particular for narrow cleft widths. Additionally, peak I_{Na} clearly depends of on the size of the cleft; the larger the cleft, the more negative is peak I_{Na} and the more prominent is the self-attenuation process.

At V_{step} = –50 mV, for F_{gNa} = 1, normalized peak I_{Na} was close to or just above 1 for all cleft geometries and all cleft widths, indicating that peak I_{Na} was comparable to peak I_{Na} in the absence of a cleft. When F_{gNa} was increased to 5.05, normalized peak I_{Na} became >>1 for narrow clefts ($\leq$50 nm). This increase was most notable for the largest cleft (R_{disc} = 11 µm). Increasing F_{gNa} further to 10.09 reinforced this effect. This indicates that increasing Na^+ channel density in the cleft membrane potentiates the self-activation process in narrow clefts. Similar to simulations with V_{step} = –25 mV, peak I_{Na} depended on cleft size, with larger clefts leading to more prominent self-activation. Interestingly, the relationship between normalized peak I_{Na} and cleft width was highly nonlinear and biphasic: when cleft width was decreased, the onset of strong self-activation depended jointly on Na^+ channel density and cleft diameter. The behaviour of peak I_{Na} in the situation of the ellipse-shaped cleft was closest to that for the disc-shaped cleft having the same radius as its semi-minor axis (2.75 µm).

The dependence of peak I_{Na} on Na^+ channel density (F_{gNa}) can be understood by examining the minimal V_e that occurs in the cleft as a function of cleft width, F_{gNa} and disc geometry for V_{step} = –25 and –50 mV, as shown in Figure 2B. The left plot of Figure 2B (F_{gNa}=1) shows that for V_{step}= –25 mV, the minimal V_e was very close to 0, even for very narrow cleft widths and a large disc-shaped cleft, for which V_e reached –20 mV. This V_e was not negative enough to decrease the driving force of I_{Na} and to cause any substantial self-attenuation. For V_{step} = –50 mV, V_e did not decrease below –2 mV and, consequently, self-activation was minimal. However, when F_{gNa} was set to 5.05 (middle plot), the negative V_e reached very negative values (up to –80 mV for R_{disc} = 11µm) for both voltage steps. A further increase of F_{gNa} to 10.09 (right plot) resulted in even more negative V_e that exceeded several tens of mV for cleft widths < 100 nm, which then led to substantial self-activation and self-attenuation, as reflected in Figure 2A.

While the dependence of self-activation and self-attenuation on Na^+ channel density is straightforward to understand, the modulation of I_{Na} by cleft size and geometry is more challenging to understand. This challenge arises from the fact that V_e is not spatially uniform in the cleft, as illustrated in Figure 2C. This panel represents the spatial profiles of V_e (at the moment of occurrence of the minimum) for $F_{gNa} = 5.05$, corresponding to the simulations shown in the middle plots in Figures 2A and 2B, for cleft widths of 20, 40 and 80 nm.

For disc-shaped clefts, the spatial V_e profiles were similar (symmetric and concave) and had a similar gradient in the periphery, especially for $V_{step} = -25$ mV. Consequently, the minimal and average V_e was larger (in absolute value) for larger discs. This larger V_e can also be explained by the fact that the radial current in the cleft had to cover a larger distance, and the associated larger resistance therefore rendered the potential difference larger, leading to stronger self-activation and self-attenuation as shown in Figure 2A. When cleft width was increased from 20 to 40 and 80 nm, V_e and its gradient became smaller (in absolute value). This can be explained by the lower radial resistance of the extracellular cleft. These results show that large disc radii and small cleft widths both favour ephaptic interactions.

For ellipse-shaped clefts, the spatial profile of V_e depends on the direction along which it is considered (major or minor axis). Along the minor axis, the profile was similar to that along the diameter of small disc-shaped clefts. This indicates that for ellipse-shaped clefts, the minimal V_e is essentially determined by the semi-minor axis, i.e., by the shortest path (of lowest resistance) to the periphery of the cleft.

Restricting the extracellular space in patch clamp experiments reveals self-attenuation and self-activation of the Na^+ current

To demonstrate self-attenuation and self-activation experimentally, we conducted patch clamp recordings of I_{Na} in HEK cells stably expressing human voltage-gated Na^+ channels detached from the growth substrate and narrowed the extracellular space near these cells by approaching them to a non-conducting obstacle, as illustrated in Figure 3A. In Figure 3B, I_{Na} is shown for one representative cell during an activation step far above activation threshold (left plot) and near the threshold (right plot), for the detached cell, the cell

approached to the obstacle and for the cell subsequently moved away. For the step far above threshold, peak I_{Na} slightly decreased (in absolute value) when the cell was approached to the obstacle, and increased back when the cell was moved away. Thus, restricting the extracellular space near a portion of the membrane reversibly attenuated I_{Na}, as predicted by the simulations (self-attenuation). In contrast, for the voltage step near the activation threshold, approaching the cell to the obstacle led to an increase in peak I_{Na}, which receded back when the cell was moved away. Restricting the extracellular space thus reversibly increased I_{Na} in agreement with the simulations (self-activation). These effects on the total I_{Na} of the cell were small, most likely because only a small fraction of the membrane was facing the obstacle.

In a series of experiments with 7 cells, a voltage-clamp activation protocol was conducted with the cell attached to the substrate, with the cell detached, with the cell approached to the obstacle and with the cell moved away from it. IV curves are shown in Figure 3C for one cell (same cell as in Figure 3B) under these four conditions. It can be noted that detaching the cell resulted in a shift of the IV relationship towards more negative potentials. The reason of this shift is unclear; possibly, the detachment of the cell and its subsequent change of shape (from flat to spherical) caused a remodelling of the cytoskeleton which, as shown in previous work (Dybkova *et al.* 2014), may affect the dynamics of Na^+ channels. However, concerning ephaptic interactions, only experiments with the detached spherical cell are pertinent. A close-up of the corresponding IV curves (insets in Figure 3B) reveals that for potentials near –20 mV and above, peak I_{Na} was reversibly decreased when the cell was approached to the obstacle, which is compatible with ephaptic self-attenuation. Conversely, for potentials near –35 mV, approaching the cell to the obstacle reversibly increased peak I_{Na}, a result strongly suggesting ephaptic self-activation of I_{Na} in the membrane in close proximity to the obstacle.

Figure 3D presents the analysis of these changes of peak I_{Na} in all 7 cells for a voltage step far above and a voltage step near threshold. Because the half activation potential ($V_{1/2}$) exhibits an intercellular variability, these two voltage steps were determined relative to the $V_{1/2}$ of each individual cell as $V_{1/2}$ +25 mV and $V_{1/2}$ –10 mV, respectively (which were rounded to the next integer multiple of the voltage step increment of 5 mV). For these two voltage steps, Figure 3D reports peak I_{Na} in the cells approached to the obstacle and in the cells subsequently moved away, normalized by corresponding peak

I_{Na} in the detached cells before approaching them to the obstacle. For voltage steps far above threshold, close proximity to the obstacle decreased peak I_{Na} in all cells (values <1). In contrast, for voltage steps near the threshold, peak I_{Na} was increased in all cells by the proximity of the obstacle (values >1). Thus, changes suggestive of ephaptic self-attenuation and self-activation were reproducibly observed in all 7 cells (p=0.0156, Wilcoxon signed rank test). The reversibility of these effects was observed in 5 out of 5 cells (in the remaining two cells, the membrane seal was lost before the last steady state activation protocol could be completed). Although the magnitude of these effects was characterized by a large intercellular variability, these results are in line with the computer simulations and in support of ephaptic interactions between V_e and I_{Na} in a narrow extracellular space.

Figure 3E shows simulated IV curves taking into account the fact that in the experiments, only a small fraction of the membrane was facing the obstacle. Assuming that the cells were spherical and that the contact with the obstacle was subtended by an angle of 90° as viewed from the cell centre, the relative areas of the membrane facing the obstacle and exposed to the bulk of the bath can be estimated to be 13% and 87%, respectively. The total I_{Na} was therefore simulated as a corresponding linear combination of I_{Na} in the presence and in the absence of the cleft. In the HEK cells, I_{Na} density was variable from cell to cell but corresponded to values of F_{gNa} between 1 and 5. Corresponding IV curves were therefore constructed for an F_{gNa} of 5.05 and 1 (Figure 3E). A good agreement with experimentally observed IV curves (see Figure 3C) was obtained with 50-100 nm wide clefts and F_{gNa}=5.05, as well as with 10-20 nm wide clefts and F_{gNa}=1.

The spatial distribution of Na$^+$ channels strongly affects ephaptic interactions

The simulations presented so far considered a homogeneous distribution of Na$^+$ channels in the disc membrane. However, recent histological studies have shown that Na$^+$ channels form clusters in intercalated discs (Rhett *et al.* 2013; Veeraraghavan *et al.* 2015; Leo-Macias *et al.* 2016). The consequences of such Na$^+$ channel clustering cannot be investigated using the HEK cells, because the distribution of Na$^+$ channels over their surface cannot be controlled and is presumably uniform.

Therefore, we took advantage of our high-resolution model and the finite element method to explore the consequences of such channel clustering on ephaptic processes. To simulate predefined spatial patterns of clustering, we modified the Na^+ current conductance in predefined regions of the disc without changing the total Na^+ current conductance of the disc membrane. This approach thus simulates a redistribution of the channels without changing the total number of channels (the total Na^+ current conductance being given by F_{gNa}).

We first investigated the effect of aggregating the Na^+ channels in one central cluster with a progressively decreasing radius (0.5, 0.25 and 0.125 times the disc radius R_{disc}), and compared the results with those obtained with a homogenous distribution (i.e., one cluster with a radius equal to R_{disc} (11 µm)), as shown in Figure 4A. For $V_{step} = -25$ mV and for narrow cleft widths, peak I_{Na} decreased when the cluster size was decreased, even with a low density of Na^+ channels ($F_{gNa} = 1$). For an F_{gNa} of 5.05, the decrease in peak I_{Na} was even stronger. This indicates that self-attenuation was stronger in the presence of smaller clusters of Na^+ channels. Conversely, for $V_{step} = -50$ mV, peak I_{Na} increased when the cluster size was decreased. This increase was accentuated when F_{gNa} was also increased. Moreover, with clusters of decreasing size, peak I_{Na} was increased over a larger range of cleft widths. Thus, self-activation was stronger with smaller clusters. These stronger effects were due to an increasingly more negative minimal V_e when the channels were arranged in the centre of the disc in a cluster of decreasing size, even with $F_{gNa}=1$. Figure 4B explains why the ephaptic effects were stronger for a small cluster by illustrating the spatial profile of V_e at the occurrence of the minimum. For the uniform Na^+ channel distribution, the profile of V_e was broad and concave. In contrast, for the Na^+ channel clusters, the V_e profiles appeared narrower and deeper (for both voltage steps), with a curvature that was different outside the cluster. Figure 4C shows that the spatial profile was hyperboloid-like outside the cluster region, while, for a uniform Na^+ channel distribution, the profile was paraboloid-like (Figure 1C). These hyperboloid-like profiles can be explained by a strongly increasing density of radial cleft current near the current sink (the Na^+ channel cluster viewed from the extracellular space) and the absence of any sink outside the cluster region. Thus, concentrating the sink into a smaller region resulted there in a more negative V_e.

Movies 3 and 4 show V_e, I_{Na} density and gating parameters for a central cluster with a radius of $0.125 \cdot R_{disc}$ for a V_{step} to –25 and –50 mV, respectively (F_{gNa}=5.05, 40 nm wide cleft). These Movies show that the time course of the gating variables (which were also computed outside the cluster but did not generate any I_{Na} there) was spatially heterogeneous, especially at a V_{step} to –50 mV (Movie 4), where *m* remained near 0 and the product *hj* near 1 in the periphery but approached respectively 1 and 0 in the cluster. This heterogeneous evolution of gating parameters was due to the particular shape of the spatial profile of V_e (Figure 4C).

Next, in Figure 4D, we examined the effect of displacing a small cluster of Na^+ channels towards the periphery. For $V_{step} = $ –25 mV and for narrow cleft widths, the decrease in I_{Na} became less prominent when the cluster was moved away towards the disc periphery, with both F_{gNa} values of 1 and 5.05. This reflects that self-attenuation was strongest when the cluster was in the centre and decreased when the cluster was moved towards the periphery. Conversely, for $V_{step} = $ –50 mV, peak I_{Na} became smaller (in absolute value) when the cluster was moved further from the centre, which indicates that self-activation was the strongest for a centred cluster. With a cluster positioned at or near the centre of the disc, peak I_{Na} was also increased over a larger range of cleft widths. Similar to the situation of decreasing cluster size (Figure 4A), these stronger ephaptic interactions were due to an increasingly more negative minimal V_e when the cluster was more central, for both F_{gNa}. Corresponding spatial V_e profiles are shown in Figures 4E and 4F. Moving the cluster towards the periphery skewed the V_e profile and rendered it asymmetric, while decreasing its minimum (in absolute value). This decrease was due to the shorter distance between the cluster and the edge of the disc, and thus to the presence of a path with a lower resistance for the radial current in the cleft.

These results show that due to the strong dependence of V_e on the spatial distribution of Na^+ channels, ephaptic effects are enhanced when Na^+ channels are aggregated into a cluster, and this enhancement is most prominent for small and central clusters.

The activation of the Na^+ current in an adjacent membrane depends on Na^+ channel cluster size and relative position

To examine ephaptic interactions between two membranes facing each other representing together an intercalated disc, and to investigate the consequences of Na^+ channel clustering on these interactions, we integrated a second excitable membrane in our computer model. The corresponding electric circuit is represented in Figure 5A. A voltage clamp activation protocol was applied on the intracellular side of the first membrane while was the potential on the intracellular side of the second membrane was held at the resting potential of –85 mV. In both membranes, two central Na^+ channel clusters with predefined radii were incorporated (Figure 5A, right) and the behaviour of I_{Na} and V_e was compared to that obtained with a uniform Na^+ channel distribution in both membranes. Note that no gap junction was incorporated at this stage.

Figure 5B shows I_{Na} flowing through the two membranes for a 20 nm wide cleft and an F_{gNa} of 5.05. Even though the intracellular side of the second membrane was clamped at –85 mV, the negative V_e, caused by the activation of I_{Na} in the first membrane led to the activation of I_{Na} in the second membrane, except in the situation of a uniform Na^+ channel distribution at $V_{step} = -25$ mV. Smaller clusters led to shorter latencies of I_{Na} activation in the second membrane. Because the intracellular side of the second membrane was held at –85 mV, V_e reached very negative values when I_{Na} was activated there. Interestingly, with small Na^+ channel clusters, these very negative V_e resulted in a transiently positive driving force for I_{Na} in the first membrane, where it produced a net outward I_{Na} current.

The response of the second membrane and the delay between the onsets of I_{Na} in the two membranes is quantified in Figure 5C. For the two membranes, the onset of I_{Na} was defined by the time at which total I_{Na} passed a predefined threshold set to 0.25% of the total I_{Na} that would be generated if all channels were open. Figure 5C reports the delay between these onsets (absent data points or curves indicate that I_{Na} in the second membrane was not activated). For $F_{gNa} = 5.05$ (assumption that 50% of Na^+ channels are located in the intercalated disc), smaller clusters and narrower clefts resulted in shorter delays. Moreover, the range of cleft widths allowing the activation of I_{Na} in the second membrane was broader for smaller clusters. For large clusters and/or wide clefts, I_{Na} was not activated in the second membrane. These relationships were observed for both voltage steps to –25 and –50 mV. When F_{gNa} was set to 1 (assumption that Na^+ channels are distributed uniformly over the entire surface of cardiomyocytes), the range of cleft widths

and cluster radii permitting I_{Na} activation in the second membrane was considerably decreased: ephaptic activation occurred only for cleft widths of 10 and 20 nm.

We next examined the effect of changing the distance between the Na^+ channel clusters in the two membranes such that the clusters are no longer facing each other. Figure 6A illustrates simulations in which one cluster (diameter: 1.375 µm = 0.125·R_{disc}) was incorporated in each membrane and the cluster centres were progressively moved away from the disc centre in opposite directions. For both step potentials, ephaptic activation of I_{Na} in the second membrane occurred only when the two clusters were co-located or in close proximity (Movies 5 and 6) but not with separations between cluster centres ≥ 5.5 um. I_{Na} activation in the second membrane caused a large additional negative deflection of V_e. This more prominently negative V_e is also visible in the spatial profiles of V_e. When I_{Na} was activated only in the first membrane, the site of the most negative V_e co-located with the cluster in the first membrane. However, when I_{Na} was also activated in the second membrane, the site of the most negative V_e co-located with the cluster in the second membrane. Interestingly, with clusters just in contact (distance between centres: 2.75 µm), total I_{Na} in the second membrane was smaller and V_e was more negative than with clusters facing each other.

The delay between the onsets of I_{Na} in the two membranes (computed as in Figure 5B) is shown in Figure 6B. For both voltage steps and for both F_{gNa}, closer distances between the clusters resulted in slightly shorter delays. However, the distance between clusters mostly determined the range of cleft widths allowing the activation of I_{Na} in the second membrane. For large distances between clusters and/or wide clefts, I_{Na} was not activated in the second membrane.

Thus, activation of I_{Na} in a second membrane is possible even when its intracellular potential is clamped at its resting value. Importantly, these results indicate that not only the density of Na^+ channels but also the spatial distribution of the channels greatly influences ephaptic I_{Na} activation, which is potentiated by small central clusters and is optimal when the clusters in the two membranes face each other.

The distribution of Na^+ channels modulates ephaptic interactions and action potential transfer between two cells coupled by a gap junctional resistance

In real cardiac tissue, cells are connected via gap junctions. Therefore, we adapted the model to investigate the interaction between ephaptic and gap junctional coupling during action potential transfer, and investigated how this transfer is influenced by the spatial distribution of Na^+ channels. As illustrated in Figure 7A, we included a gap junctional resistance connecting the intracellular space of the two cells. In addition, we added on both sides of the intercalated disc an excitable element representing the bulk membranes of the cells (100 µm long cylinders with a radius of 11 µm). This arrangement permitted to conduct simulations under current clamp conditions of the intracellular nodes. Numerically, this was done by considering the two intracellular potentials as additional variables and by adding to the matrices **K** and **M** (see Methods) two rows/columns constructed in accordance with charge conservation (Kirchhof current law). To elicit an action potential in the first cell, a rectangular current pulse was applied. The cleft width was 30 nm and an F_{gNa} of 5.05 was used. Gap junctional coupling was varied from a normal level of 100% (1.5 Ωcm^2 (Shaw & Rudy 1997)) to 0%.

Simulations were conducted for three scenarios: a uniform Na^+ channel distribution in both intercalated disc membranes, two aligned central Na^+ channel clusters, and two misaligned Na^+ channel clusters. The corresponding intracellular potentials (V_i) are shown in Figure 7B for three levels of gap junctional coupling (100%, 5% and 0%). The corresponding I_{Na} in the bulk and disc membranes are shown in Figure 7C and the corresponding V_e in Figure 7D.

When the Na^+ channels were uniformly distributed in the disc (first column), the second cell was not excited when the coupling level was 0 and ephaptic coupling alone was not sufficient to activate the second cell. Indeed, the V_e caused by the I_{Na} of the first disc was >–20 mV. The second cell was however excited at a coupling level of 5% after a delay of 0.4 ms (computed from the interval between the 0 mV crossings of the upstrokes). However, action potential transmission was essentially electrotonic because V_e caused by the I_{Na} of the first disc was also >–25 mV. At the normal coupling level, the cells were activated electrotonically and quasi synchronously due to the large coupling conductance. In contrast, when two aligned central Na^+ channel clusters were simulated (second column), the second cell was activated by ephaptic interactions in the absence of coupling after a delay of 1.2 ms. Again, at a coupling level of 100%, action potential transfer was electrotonic and the upstrokes were almost synchronous. However, at a reduced but

nonzero level of coupling (5%), the aggregation of Na^+ channels into central clusters facing each other led to ephaptic interactions that were sufficient to shorten the activation delay from 0.4 to 0.3 ms. This contribution of ephaptic interactions is witnessed by V_e reaching values <-50 mV and by the fact that I_{Na} in the second disc peaked *before* I_{Na} in the bulk membrane of the second cell. This I_{Na} in the second disc contributed to depolarize the bulk membrane of the second cell to threshold. When the clusters were misaligned (third column), these ephaptic interactions diminished. In the absence of gap junctional coupling, the second cell was no longer excited, and at a coupling level of 5%, the activation delay increased.

The effects of ephaptic coupling on the intercellular activation delay and the dependence of the delay on cleft width are summarized in Figure 7E. For the uniform Na^+ channel distribution and for the case of misaligned clusters, ephaptic effects only slightly shortened this delay (almost superimposed curves), and action potential transfer was therefore essentially electrotonic. However, in the case of aligned clusters, ephaptic interactions in 10-30 nm clefts clearly shortened the delay for coupling levels $\leq$5%. These observations indicate that the distribution of Na^+ channels greatly influences the ephaptic interactions and action potential transfer between two cells with a reduced gap junctional coupling.

Discussion

Although already proposed decades ago (Sperelakis & Mann 1977), the existence of ephaptic interactions in the heart and the possibility of cardiac ephaptic conduction are still controversial. In this work, we report two findings that are in support of ephaptic interactions. First, we provide an experimental demonstration using patch clamp experiments that ephaptic effects near a cell membrane containing human cardiac Na^+ channels can modulate the Na^+ current in a manner predicted by computer simulations. Second, using a new FEM model, we show that the aggregation of Na^+ channels into clusters greatly potentiates ephaptic effects, a finding which is of importance in the light

of recent studies that demonstrate such Na^+ channel clustering in intercalated discs (Leo-Macias *et al.* 2016), notably in the perinexus (Rhett *et al.* 2013; Veeraraghavan *et al.* 2015).

In our patch clamp experiments with HEK cells expressing $Na_v1.5$ channels, we systematically observed that restricting the extracellular space near a part of the cell membrane causes two phenomena. At potentials far above the threshold, peak I_{Na} was decreased by this intervention (self-attenuation), whereas at potentials near the threshold, peak I_{Na} was increased (self-activation), in agreement with present and past simulation studies (Kucera *et al.* 2002; Tsumoto *et al.* 2011). These findings at the cellular level provide a proof-of-principle in favour of the existence of cardiac ephaptic effects. Noteworthy, the magnitude of these effects was characterized by a large intercellular variability. Here, it must first be noted that the level of Na^+ channel expression also exhibited intercellular variability (densities corresponding to F_{gNa} in the range 1-5). Second, the size of the region in contact with the obstacle was not controllable precisely. Third, the width of the cleft was not known, and could also have been variable. As shown in Figure 2, these three parameters determine jointly the magnitude of the effects on peak I_{Na} in a nonlinear manner. Thus, the variable magnitude of the ephaptic effects observed experimentally can be explained by the variability of these three parameters and the difficulty to control them.

The simulations demonstrate that the spatial distribution of Na^+ channels in two closely apposed excitable membranes exerts a crucial influence on ephaptic interactions. Specifically, our results indicate that the presence of Na^+ channel clusters facing each other across the intercellular cleft potentiates ephaptic impulse transmission when intercellular coupling is reduced. This potentiation is due to the intricate spatiotemporal dynamic interactions between I_{Na}, V_e, and Na^+ channel gating, as revealed by our high-resolution modelling approach.

Ephaptic effects are spatially heterogeneous

In particular, our simulations demonstrated that V_e in the cleft space varies as a function of position with the cleft. Even with a homogeneous distribution of Na^+ channels, the changes in V_e were minimal near the junction of the cleft and the bulk extracellular space,

and maximal near the centre of the cleft. This observation is in line with the previous results of Mori, Fishman and Peskin (Mori *et al.* 2008), who examined the spatial profiles of V_e in a model of ephaptic conduction assuming a radial symmetry of the cleft. As a consequence of this spatially variable V_e, the effects of V_e on Na^+ channel gating are not uniform but occur with different intensities and kinetics that depend on the position in the cleft, as visible in Figure 1. Because V_e also directly determines the driving force of I_{Na}, the resulting spatial distribution of I_{Na} density is also influenced. Thus, an important finding of our study is that ephaptic effects (both self-activation and self-attenuation) are spatially heterogeneous.

It therefore appears logical that the spatiotemporal interaction between V_e, I_{Na} and channel gating is further determined by the distribution of Na^+ channels. Changing this distribution directly influences the spatial pattern of V_e, rendering it more negative at locations with increased Na^+ channel density. Consequently, because of the feedback of V_e on I_{Na}, the characteristic ephaptic interactions are potentiated at and near the cluster locations (Figures 4 and 5).

The physiological relevance of Na^+ channel clusters and perinexi

Because V_e affects Na^+ channel function on both sides of an intercellular cleft, ephaptic coupling and ephaptic conduction across an intercalated disc are determined by the distribution of Na^+ channels on both membranes. We found that ephaptic coupling is optimized by small Na^+ channel clusters facing each other across the cleft space (Figures 6 and 7). This finding therefore strongly supports the notion that the localization of Na^+ channels in the perinexus has a functional electrophysiological relevance, as proposed by Rhett and co-workers (Rhett & Gourdie 2012; Rhett *et al.* 2013). We therefore postulate that perinexi are privileged sites for ephaptic coupling in pathological situations where gap junctional coupling is decreased, e.g., consecutive to intracellular acidification and Ca^{2+} overload during ischemia, or resulting from changes in connexin phosphorylation levels. Consequently, we suggest that any disease or clinical condition leading to a disruption of the perinexal arrangement of Na^+ channels may have repercussions on cardiac conduction.

The fact that Na^+ channels form clusters in the intercalated disc was recently ascertained by Leo-Macias et al. (Leo-Macias *et al.* 2016). However, it was not established on what side of the intercalated disc these clusters were located. The question is therefore still open whether Na^+ channels form clusters on corresponding face-to-face locations of the intercalated disc. Such co-localization could occur even in regions remote from gap junction plaques, possibly with the facilitation of structural proteins. It is hoped that further morphological studies will provide additional elements pertinent to the physiological role of Na^+ channel distribution.

Comparison with previous studies

To date, experimental studies aiming at proving or disproving cardiac ephaptic coupling are scarce. Suenson (Suenson 1984) investigated interactions between two trabeculae or papillary muscles tightly apposed side by side and demonstrated that excitation of one preparation can induce the excitation of the other when the width of the extracellular solution layer was narrowed. However, in experiments with patch-clamped isolated myocytes, Weingart and Maurer (Weingart & Maurer 1988) did not observe ephaptic impulse transmission when two isolated myocytes were gently brought in close lateral contact. At that time, the increased density of Na^+ channels in intercalated discs was not yet known, and no experiments were conducted with cells brought in longitudinal contact. The insufficient density of Na^+ channels in the lateral membranes may therefore explain the absence of ephaptic interactions in these experiments.

The involvement of ephaptic interactions in cardiac conduction was investigated in a series of studies combining optical mapping of impulse propagation in whole hearts by Poelzing's group and mathematical modelling of conduction with ephaptic interactions by Lin and Keener (Lin & Keener 2010, 2013, 2014; George *et al.* 2015; Veeraraghavan *et al.* 2015; Veeraraghavan *et al.* 2016). It was found that Na^+ channel blockers, gap junctional uncouplers and changes in extracellular Na^+ and K^+ concentrations, in conjunction with interventions modifying the width of the intercellular space, exerted effects on conduction velocity and its anisotropy ratio that cannot be explained by electrotonic coupling alone, thus providing support for the involvement of ephaptic interactions in intact tissue.

In contrast, observations in disfavour of ephaptic conduction were reported by Kléber's group, who investigated conduction in cultured strands of homozygous connexin 43 knock-out murine ventricular myocytes (Beauchamp *et al.* 2004). These preparations exhibited very slow conduction (2.1 cm/s vs. 52 cm/s in wild type strands), which was attributed to a low level of connexin 45 expression. Exposing the knock-out strands to the gap junctional uncoupler heptanol abolished conduction completely. However, it must here be noted that according to our findings, the shape of intercellular contacts greatly influences ephaptic interactions. Figure 2 shows that when the excitable disc is given an elongated shape, the magnitude of ephaptic effects is drastically reduced because they are essentially determined by the smallest dimension across this shape. The fact that cultured cardiomyocytes flatten on the growth substrate and assume a thickness of only a few μm (Jousset *et al.* 2016) therefore renders ephaptic conduction unlikely in such preparations. These considerations can explain the absence of ephaptic conduction in experiments with cultures of cardiomyocytes and suggest that such preparations are not an appropriate experimental model to study ephaptic impulse transmission.

Limitations

It could be argued why we did not compare I_{Na} in cells attached to the substrate to I_{Na} in detached cells, given the fact that in attached cells, the extracellular space between the cell and the substrate is also confined. However, detaching the cell involves a change in cell shape and thus a likely remodelling of the cytoskeletal architecture, which is known to influence the biophysical properties of I_{Na} (Dybkova *et al.* 2014). In addition, such a protocol would not permit to examine whether changes in I_{Na} are reversible. For these reasons, we preferred to develop a protocol in which the change in cell shape is negligible and in which the extracellular space can be restricted rapidly and with minimal interference with the cell.

Beyder et al. (Beyder *et al.* 2010; Beyder *et al.* 2012) have shown in HEK cells expressing $Na_v1.5$ channels that applying negative pressure to cell-attached patches leads to an increase in I_{Na}. This mechanosensitivity of Na^+ channels may have increased I_{Na} in our experiments when the cells were approached to the obstacle. However, such an increase would pertain to all depolarizing step potentials, both near threshold and far above

threshold. The fact that we systematically observed a decrease in I_{Na} at potentials far above threshold indicates that another mechanism must have been involved. Although we did not observe any membrane deformation, we cannot fully exclude the possibility that at potentials near threshold, minor mechanical effects contributed to the increase in I_{Na}, in addition to ephaptic self-activation.

In the simulations, we did not consider tortuous intercalated disc shapes as observed in vivo (Leo-Macias *et al.* 2015) or heterogeneities of cleft width. Tortuosity is expected to strengthen ephaptic effects by increasing the effective radial resistance of the cleft. Regions of narrow cleft width are also expected to reinforce ephaptic interactions, in particular in the presence of Na^+ channels, as in the perinexus. We also assumed that the intracellular potential is spatially uniform, and it was therefore not possible to assess the effects of different distributions of gap junctions. Such analysis would require the development of an explicit three-dimensional modelling framework. This development was however beyond the scope of our study. Furthermore, because of the high computational expense of high-resolution models, we did not investigate conduction in cell fibres but preferred to focus on resolving spatial features at the level of the single disc. Finally, we used a simplified membrane model incorporating only I_{Na} and a linear K^+ current. Although this model did not take other currents or calcium dynamics into account, it offered the advantage to isolate the specific role of I_{Na} in ephaptic interactions without any confounding factors. All these considerations open prospects for further studies.

Conclusions

Our findings provide new insights into basic mechanisms of cardiac excitation and conduction and highlight the usefulness of the new mathematical model of the intercalated disc that we developed. By contributing to understanding the structure and function of the intercalated disc, our results may orient future experimental and modelling work to better encompass under what conditions ephaptic interactions may influence cardiac electrical function in the healthy and diseased heart.

References

Beauchamp P, Choby C, Desplantez T, de Peyer K, Green K, Yamada KA, Weingart R, Saffitz JE & Kléber AG (2004). Electrical propagation in synthetic ventricular myocyte strands from germline connexin 43 knockout mice. *Circ Res* 95, 170-178.

Beyder A, Rae JL, Bernard C, Strege PR, Sachs F & Farrugia G (2010). Mechanosensitivity of Na$_v$1.5, a voltage-sensitive sodium channel. *J Physiol* 588, 4969-4985.

Beyder A, Strege PR, Reyes S, Bernard CE, Terzic A, Makielski J, Ackerman MJ & Farrugia G (2012). Ranolazine decreases mechanosensitivity of the voltage-gated sodium ion channel Na$_v$1.5: a novel mechanism of drug action. *Circulation* 125, 2698-2706.

Cohen SA (1996). Immunocytochemical localization of rH1 sodium channel in adult rat heart atria and ventricle. Presence in terminal intercalated disks. *Circulation* 94, 3083-3086.

Crank J & Nicholson P (1947). A practical method for numerical evaluation of solutions of partial differential equations of the heat conduction type. *Proc Cambridge Phil Soc* 43, 50-67.

Dhar Malhotra J, Chen C, Rivolta I, Abriel H, Malhotra R, Mattei LN, Brosius FC, Kass RS & Isom LL (2001). Characterization of sodium channel alpha- and beta-subunits in rat and mouse cardiac myocytes. *Circulation* 103, 1303-1310.

Dolber PC, Beyer EC, Junker JL & Spach MS (1992). Distribution of gap junctions in dog and rat ventricle studied with a double-label technique. *J Mol Cell Cardiol* 24, 1443-1457.

Dybkova N, Wagner S, Backs J, Hund TJ, Mohler PJ, Sowa T, Nikolaev VO & Maier LS (2014). Tubulin polymerization disrupts cardiac beta-adrenergic regulation of late I$_{Na}$. *Cardiovasc Res* 103, 168-177.

George SA, Sciuto KJ, Lin J, Salama ME, Keener JP, Gourdie RG & Poelzing S (2015). Extracellular sodium and potassium levels modulate cardiac conduction in mice heterozygous null for the Connexin43 gene. *Pflugers Arch* 467, 2287-2297.

Gutstein DE, Morley GE, Tamaddon H, Vaidya D, Schneider MD, Chen J, Chien KR, Stuhlmann H & Fishman GI (2001). Conduction slowing and sudden arrhythmic death in mice with cardiac-restricted inactivation of connexin43. *Circ Res* 88, 333-339.

Johnson C (1987). Numerical solution of partial differential equations by the finite element method. Cambridge University Press / Dover.

Jousset F, Maguy A, Rohr S & Kucera JP (2016). Myofibroblasts electrotonically coupled to cardiomyocytes alter conduction: insights at the cellular level from a detailed in silico tissue structure model. *Front Physiol* 7, 496.

Kléber AG & Rudy Y (2004). Basic mechanisms of cardiac impulse propagation and associated arrhythmias. *Physiol Rev* 84, 431-488.

Kucera JP, Rohr S & Rudy Y (2002). Localization of sodium channels in intercalated disks modulates cardiac conduction. *Circ Res* 91, 1176-1182.

Leo-Macias A, Agullo-Pascual E, Sanchez-Alonso JL, Keegan S, Lin X, Arcos T, Feng Xia L, Korchev YE, Gorelik J, Fenyo D, Rothenberg E, Rothenberg E & Delmar M (2016). Nanoscale visualization of functional adhesion/excitability nodes at the intercalated disc. *Nat Commun* 7, 10342.

Leo-Macias A, Liang FX & Delmar M (2015). Ultrastructure of the intercellular space in adult murine ventricle revealed by quantitative tomographic electron microscopy. *Cardiovasc Res* 107, 442-452.

Lin J & Keener JP (2010). Modeling electrical activity of myocardial cells incorporating the effects of ephaptic coupling. *Proc Natl Acad Sci USA* 107, 20935-20940.

Lin J & Keener JP (2013). Ephaptic coupling in cardiac myocytes. *IEEE Trans Biomed Eng* 60, 576-582.

Lin J & Keener JP (2014). Microdomain effects on transverse cardiac propagation. *Biophys J* 106, 925-931.

Lin X, Liu N, Lu J, Zhang J, Anumonwo JM, Isom LL, Fishman GI & Delmar M (2011). Subcellular heterogeneity of sodium current properties in adult cardiac ventricular myocytes. *Heart Rhythm* 8, 1923-1930.

Livshitz L & Rudy Y (2009). Uniqueness and stability of action potential models during rest, pacing, and conduction using problem-solving environment. *Biophys J* 97, 1265-1276.

Luo CH & Rudy Y (1991). A model of the ventricular cardiac action potential. Depolarization, repolarization, and their interaction. *Circ Res* 68, 1501-1526.

Luo CH & Rudy Y (1994). A dynamic model of the cardiac ventricular action potential. I. Simulations of ionic currents and concentration changes. *Circ Res* 74, 1071-1096.

Maier SK, Westenbroek RE, Schenkman KA, Feigl EO, Scheuer T & Catterall WA (2002). An unexpected role for brain-type sodium channels in coupling of cell surface depolarization to contraction in the heart. *Proc Natl Acad Sci USA* 99, 4073-4078.

Mori Y, Fishman GI & Peskin CS (2008). Ephaptic conduction in a cardiac strand model with 3D electrodiffusion. *Proc Natl Acad Sci USA* 105, 6463-6468.

Rhett JM & Gourdie RG (2012). The perinexus: a new feature of Cx43 gap junction organization. *Heart Rhythm* 9, 619-623.

Rhett JM, Veeraraghavan R, Poelzing S & Gourdie RG (2013). The perinexus: sign-post on the path to a new model of cardiac conduction? *Trends Cardiovasc Med* 23, 222-228.

Rush S & Larsen H (1978). A practical algorithm for solving dynamic membrane equations. *IEEE Trans Biomed Eng* 25, 389-392.

Shaw RM & Rudy Y (1997). Ionic mechanisms of propagation in cardiac tissue. Roles of the sodium and L-type calcium currents during reduced excitability and decreased gap junction coupling. *Circ Res* 81, 727-741.

Shy D, Gillet L & Abriel H (2013). Cardiac sodium channel $Na_v1.5$ distribution in myocytes via interacting proteins: the multiple pool model. *Biochim Biophys Acta* 1833, 886-894.

Sperelakis N (2002). An electric field mechanism for transmission of excitation between myocardial cells. *Circ Res* 91, 985-987.

Sperelakis N & Mann JE, Jr. (1977). Evaluation of electric field changes in the cleft between excitable cells. *J Theor Biol* 64, 71-96.

Suenson M (1984). Ephaptic impulse transmission between ventricular myocardial cells in vitro. *Acta Physiol Scand* 120, 445-455.

Sundnes J, Lines GT, Cai X, Nielsen BF, Mardal KA & Tveito A (2006). Computing the electrical activity in the heart. Springer Berlin Heidelberg New York.

Tsumoto K, Ashihara T, Haraguchi R, Nakazawa K & Kurachi Y (2011). Roles of subcellular Na^+ channel distributions in the mechanism of cardiac conduction. *Biophys J* 100, 554-563.

van Rijen HV, Eckardt D, Degen J, Theis M, Ott T, Willecke K, Jongsma HJ, Opthof T & de Bakker JM (2004). Slow conduction and enhanced anisotropy increase the propensity for ventricular tachyarrhythmias in adult mice with induced deletion of connexin43. *Circulation* 109, 1048-1055.

Veeraraghavan R, Lin J, Hoeker GS, Keener JP, Gourdie RG & Poelzing S (2015). Sodium channels in the Cx43 gap junction perinexus may constitute a cardiac ephapse: an experimental and modeling study. *Pflugers Arch* 467, 2093-2105.

Veeraraghavan R, Lin J, Keener JP, Gourdie R & Poelzing S (2016). Potassium channels in the Cx43 gap junction perinexus modulate ephaptic coupling: an experimental and modeling study. *Pflugers Arch* 468, 1651-1661.

Veeraraghavan R, Poelzing S & Gourdie RG (2014). Old cogs, new tricks: a scaffolding role for connexin43 and a junctional role for sodium channels? *FEBS Lett* 588, 1244-1248.

Vermij SH, Abriel H & van Veen TA (2017). Refining the molecular organization of the cardiac intercalated disc. *Cardiovasc Res* 113, 259-275.

Wei N, Mori Y & Tolkacheva EG (2016). The dual effect of ephaptic coupling on cardiac conduction with heterogeneous expression of connexin 43. *J Theor Biol* 397, 103-114.

Weidmann S (1970). Electrical constants of trabecular muscle from mammalian heart. *J Physiol* 210, 1041-1054.

Weingart R & Maurer P (1988). Action potential transfer in cell pairs isolated from adult rat and guinea pig ventricles. *Circ Res* 63, 72-80.

Additional information

Competing interests

The authors have no competing interests to disclose.

Author contributions

J.P.K. conceived and designed the study. E.H. conducted patch clamp experiments. J.P.K. and E.H. developed simulation code and conducted simulations. E.H. and J.P.K. analysed the data. H.A. provided advice and support in conducting the experiments and interpreting

the data. E.H. and J.P.K. drafted the manuscript. All authors contributed to the interpretation of the data and to a critical review of the manuscript for important intellectual content.

All authors approved the final version of the manuscript, agree to be accountable for all aspects of the work in ensuring that questions related to the accuracy or integrity of any part of the work are appropriately investigated and resolved and all persons designated as authors qualify for authorship, and all those who qualify for authorship are listed.

Translational perspective

Cardiac conduction disorders can result in arrhythmias, which are frequent and potentially life-threatening complications of heart disease. Conduction relies on membrane depolarization by the sodium (Na^+) current (I_{Na}) and on intercellular electrical coupling via gap junctions. Recent studies showed that Na^+ channel density is high in intercalated discs and that Na^+ channels aggregate near gap junctional plaques in regions called perinexi. These findings raised the interest for another mechanism that could contribute to conduction, called ephaptic coupling. According to this mechanism, I_{Na} through the membrane on one side of the intercalated disc causes a substantial negative extracellular potential in the narrow intercellular cleft. This negative V_e translates as membrane

depolarization on the other side of the disc, where it contributes to Na^+ channel activation and thus to conduction. However, ephaptic conduction is still controversial. We conducted proof-of-principle experiments with cells expressing human cardiac Na^+ channels to demonstrate that cardiac I_{Na} is modulated by ephaptic interactions when the extracellular space is restricted. Using a high-resolution model of the intercalated disc, we found that ephaptic impulse transmission from one cell to another is facilitated by clusters of Na^+ channels facing each other across the intercellular cleft when gap junctional coupling is reduced. Our work contributes to the general understanding of cardiac excitation and indicates that perinexi are important functional elements for ephaptic coupling in pathological situations where gap junctional coupling is decreased. Conditions leading to a rearrangement of Na^+ channels in intercalated discs may therefore have repercussions on cardiac conduction.

Number of words: 248

Figure 1. Dynamical interactions between I_{Na} and V_e in a disc-shaped membrane (radius: 11 µm) separated from a non-conducting obstacle by an extracellular cleft (uniform distribution of g_{Na}, $F_{gNa}=10.09$).
A: Schematic of the model (*left:* cross section; *middle:* finite element mesh) with membrane capacitance, ion currents and extracellular resistive properties (blue). V_e at the rim of the disc was held at 0 (red). Due to radial symmetry (uniform Na⁺ channel distribution), the model behaviour does not depend on the azimuthal coordinate but only on the radial coordinate (*right*). B: *Left:* Total I_{Na} during an activation step from –85 mV to –25 mV (top) and to –50 mV (bottom), for various cleft widths. *Middle:* Corresponding colour maps of V_e, I_{Na}, gate *m* and gate product *hj* as a function of time and distance from the centre, for a 20 nm wide cleft. C: Spatial profile of V_e at the occurrence of the minimum (arrow in the middle panel) for V_{step} = –25 mV and a cleft width of 20 nm. D: Minimal V_e registered in the cleft as a function of cleft width, for V_{step} = –25 mV and –50 mV. Note the abrupt behaviour for V_{step} =–50 mV (blue arrow). E: Relationship between peak total I_{Na} and V_{step} for various cleft widths (left) and derived steady-state activation curves (right).
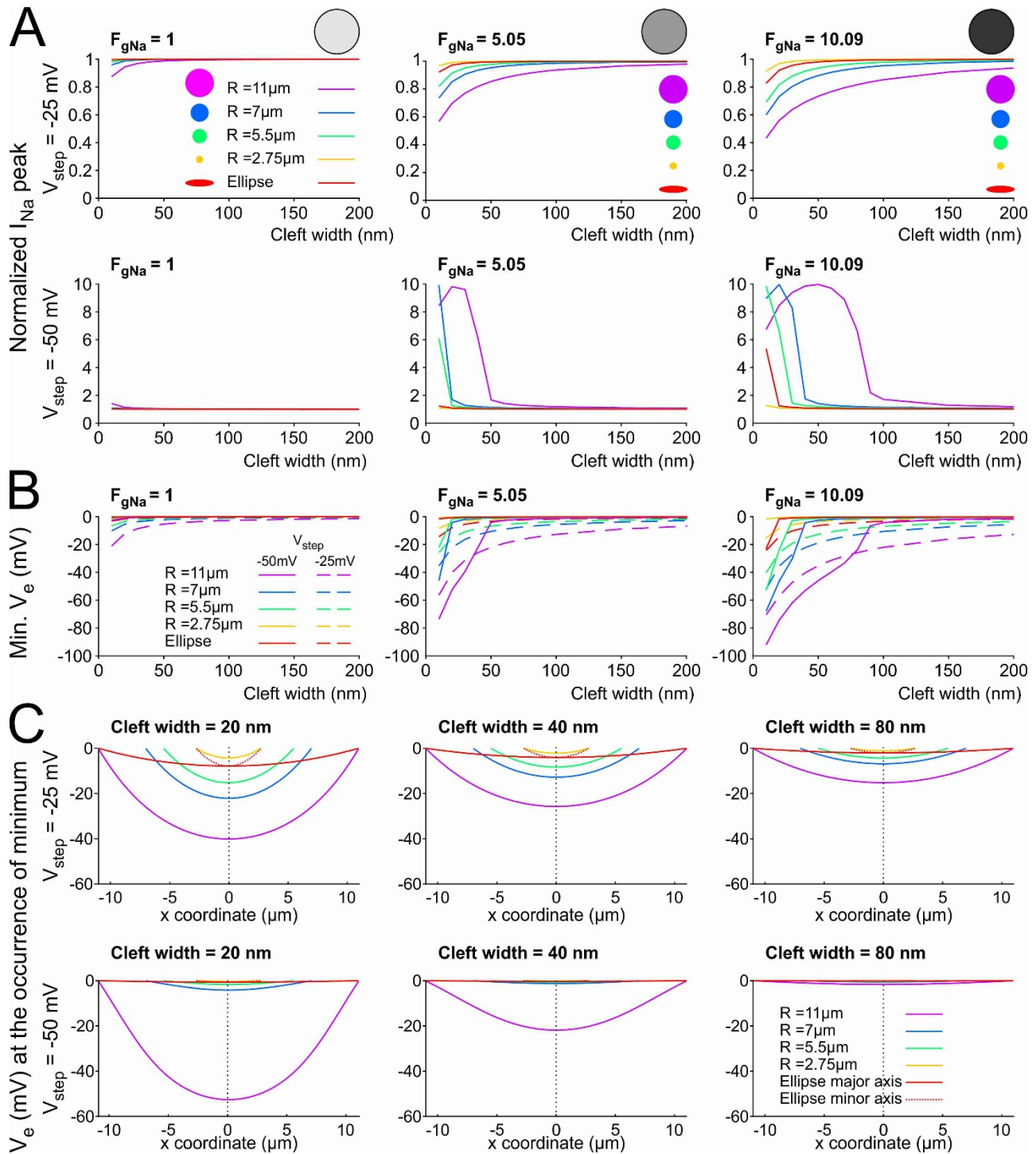
Figure 2. Effects of cleft size, cleft geometry and Na$^+$ channel density on peak I$_{Na}$ and V$_e$ for a membrane separated from a non-conducting obstacle by an extracellular cleft (uniform distribution of g$_{Na}$).
A: Peak I$_{Na}$ (normalized by peak I$_{Na}$ in the absence of a cleft) as a function of cleft width for different disc-shaped clefts (radii: see colour legend) and an elliptic cleft (semi-major axis: 11 μm, semi-minor axis: 2.75 μm), at V$_{step}$ = –25 mV (*top*) and –50 mV (*bottom*), for F$_{gNa}$=1 (*left*), F$_{gNa}$=5.05 (*middle*) and F$_{gNa}$=10.09 (*right*). B: Corresponding minimal V$_e$ (dashed lines: V$_{step}$ = –25 mV; full lines: V$_{step}$ = –50 mV). C: Corresponding spatial profiles of V$_e$ along the cleft diameter (or major/minor axis) at the occurrence of the minimum, for F$_{gNa}$=5.05, at V$_{step}$ = –25 mV (*top*) and –50 mV (*bottom*), and for cleft widths of 20 nm (*left*), 40 nm (*middle*) and 80 nm (*right*).
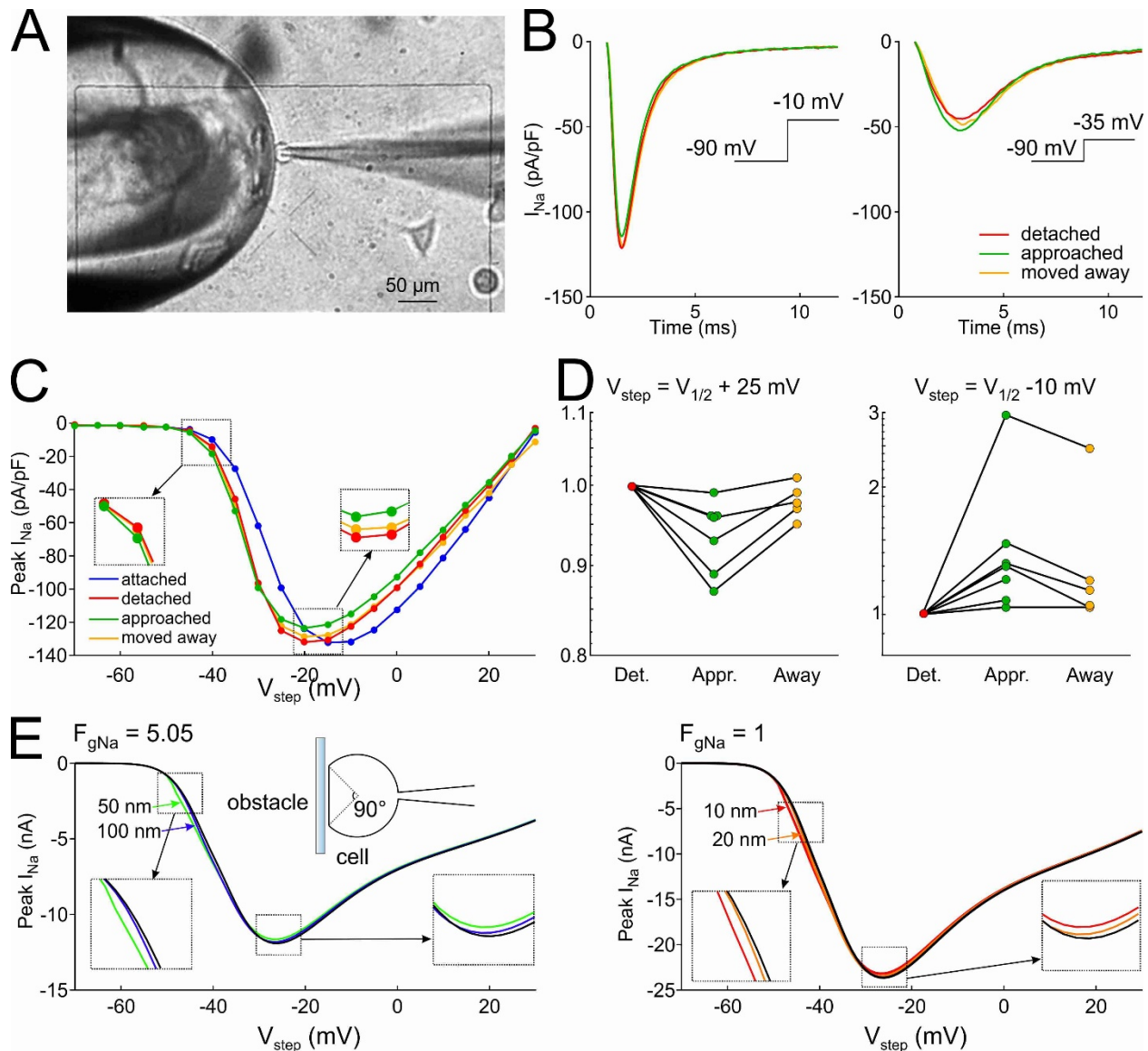
Figure 3. Experimental evidence of ephaptic effects in patch clamped HEK cells
A: Phase contrast microphotograph of a patch clamped HEK cell (pipette visible on the right) detached from its growth substrate and approached to a non-conducting glass obstacle (left). B: I_{Na} recorded from the same cell during an activation step to -10 mV (far above threshold, *left*) and to -35 mV (near the activation threshold, *right*) under following conditions; detached cell (red), cell approached to the obstacle (green) and cell subsequently moved away (yellow). C: IV curves of the same cell under these three conditions as well as for the cell still attached to the growth substrate (blue). Insets illustrate the IV curves near and far above the threshold. D: Peak I_{Na} recorded in cells (n=7) approached to the obstacle and in cells subsequently moved away normalized by corresponding peak I_{Na} in the detached cells before approaching them to the obstacle, for an activation step far above threshold (to $V_{1/2}+25$ mV, *left*) and near the activation threshold (to $V_{1/2}-10$ mV, *right*). Lines connect measurements in the same cell. E: Simulated IV curves using an F_{gNa} of 5.05 and cleft widths of 50 and 100 nm (*left*) and an F_{gNa} of 1 and cleft widths of 10 and 20 nm (*right*), assuming that the contact with the obstacle is subtended by an angle of 90° from the cell centre (schematic). $R_{disc}=11$ µm. Insets illustrates the IV curves near and far above the threshold.
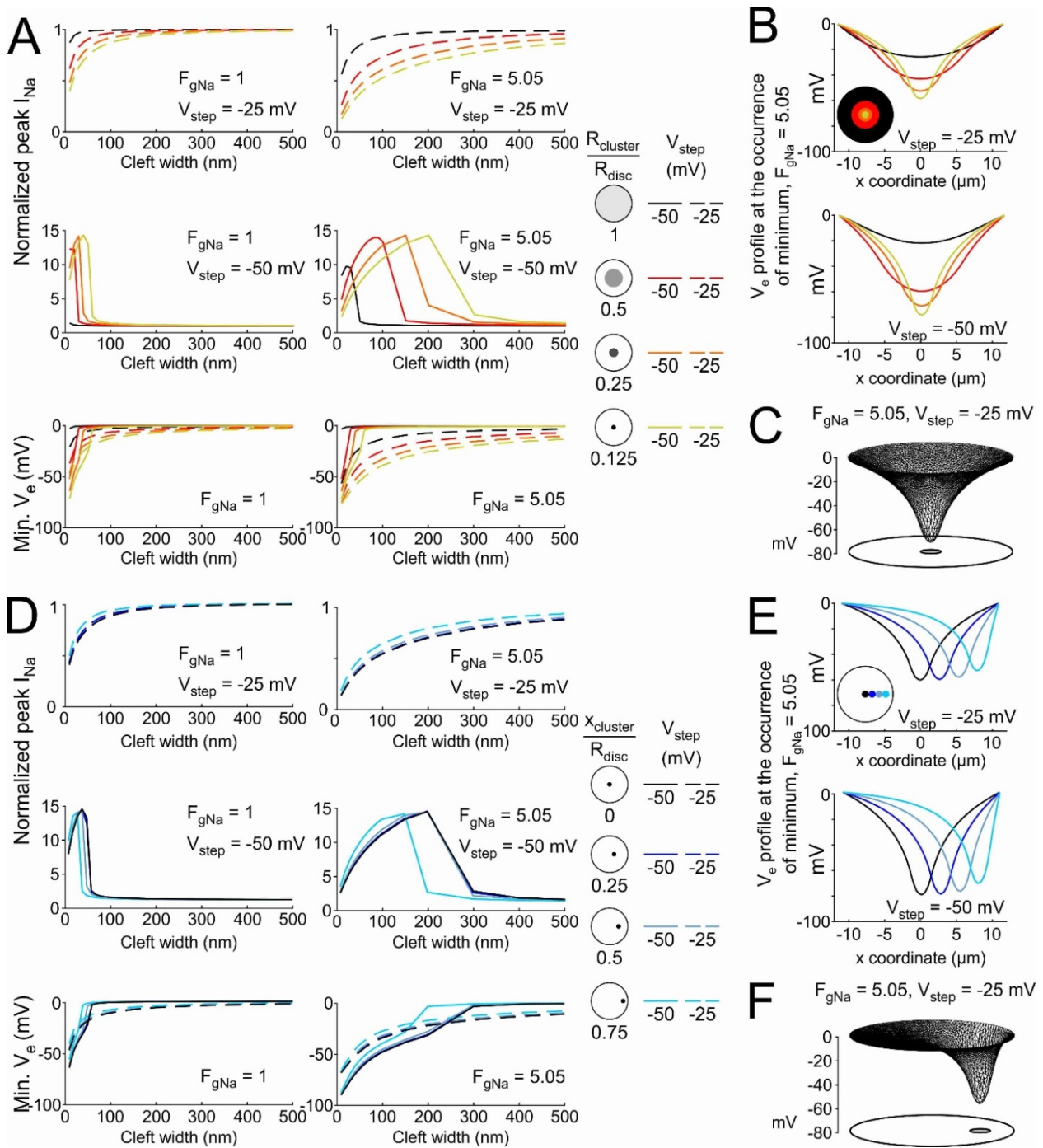
Figure 4. Effects of Na+ channel clustering on ephaptic interactions in a disc-shaped membrane (radius: R_{disc}=11 μm) separated from a non-conducting obstacle by an extracellular cleft.
A: *Top and middle:* Peak I_{Na} (normalized by peak I_{Na} in the absence of a cleft) as a function of cleft width for $V_{step} = -25$ mV (*left*) and –50 mV (*right*). Data are shown for different Na+ channel cluster sizes (cluster radius 1x (control uniform distribution), 0.5x, 0.25x and 0.125x that of R_{disc}, as shown on the *right*) with $F_{gNa} = 1$ (*left*) and $F_{gNa} = 5.05$ (*right*). *Bottom:* Corresponding minimal V_e as a function of cleft width for $V_{step} = -25$ mV (dashed lines) and $V_{step} = -50$ mV (full lines) for $F_{gNa} = 1$ (*left*) and $F_{gNa} = 5.05$ (*right*). B: Spatial V_e profiles along the disc diameter (x-coordinate) at the occurrence of the minimum (F_{gNa}=5.05; cleft width: 40 nm), for different concentric Na+ channel cluster sizes (as in A), for $V_{step} = -25$ mV (*top*) and – 50mV (*bottom*). C: Mesh of V_e at the occurrence of the minimum for a cleft width of 40 nm, a V_{step} to –25 mV, and an F_{gNa} of 5.05, for a central cluster having a radius of $0.125 \cdot R_{disc}$. D: Same as A, but for a Na+ channel cluster with a radius 0.125 times that of the disc membrane positioned at increasing distances from the centre (ratio of the x-coordinate of the cluster centre ($x_{cluster}$) to R_{disc}, legend on the right). E: Same as B, but for different positions of a small cluster with a radius of $0.125 \cdot R_{disc}$ (as in D). F: Same as C, but for a cluster (radius: $0.125 \cdot R_{disc}$) shifted towards the periphery ($x_{cluster}$: $0.75 \cdot R_{disc}$).
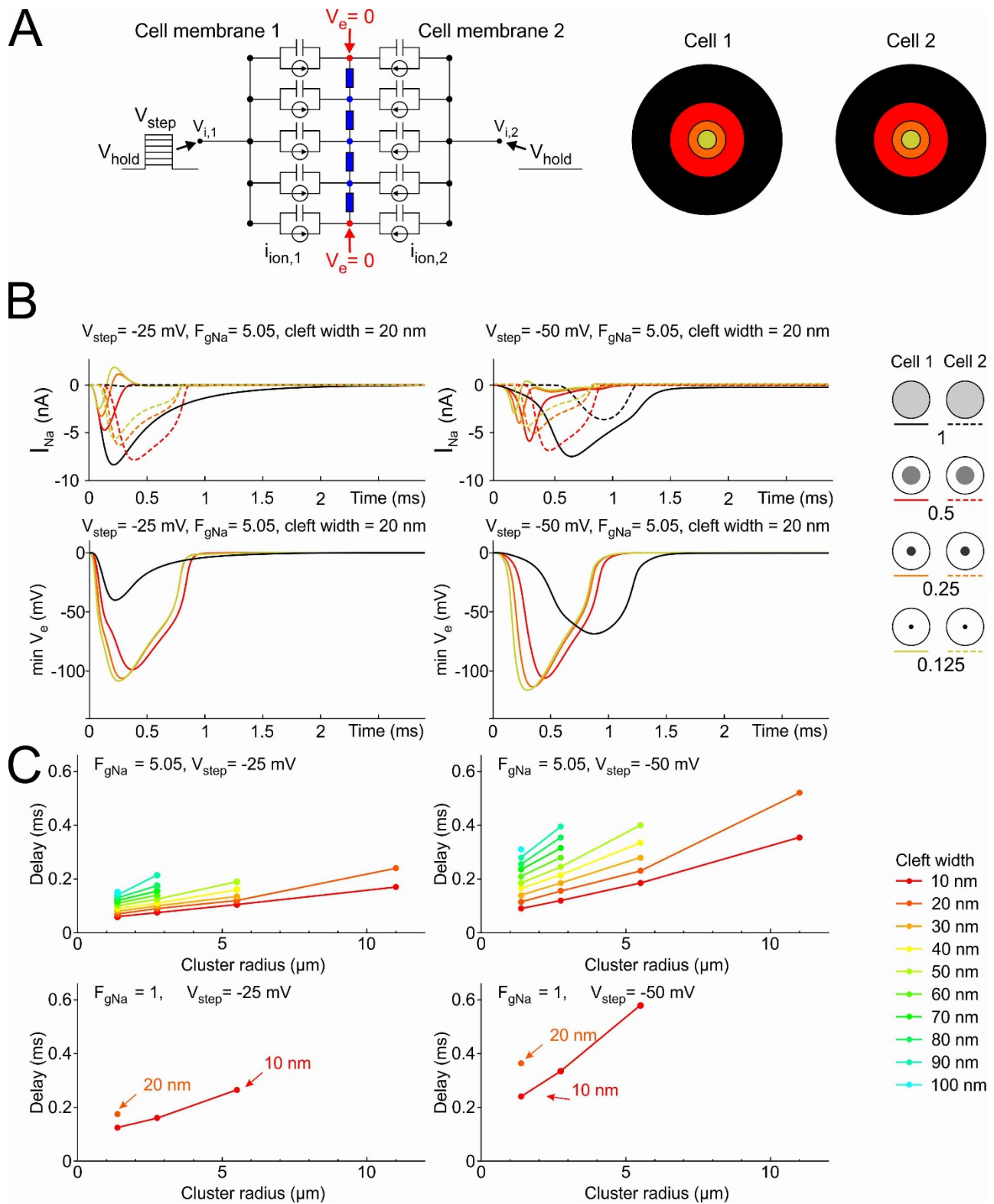
Figure 5. Effects of Na⁺ channel cluster size on I_{Na} and V_e in two membranes separated by a narrow cleft (R_{disc}=11 μm)

A: *Left:* Schematic of the two-membrane model with membrane capacitance, ion currents and extracellular resistive properties. *Right:* Schematic of the two membranes containing each a central cluster of a given radius (1x (control uniform distribution), 0.5x, 0.25x and 0.125x that of R_{disc}). B: *Top*: Total I_{Na} in membrane 1 (full lines) and membrane 2 (dashed lines) as a function of time, for different cluster radii (legend) and a 20 nm wide cleft, for a V_{step} to –25 mV (left) and –50 mV (right). *Bottom*: Corresponding time courses of minimal V_e for a V_{step} to –25 mV (left) and –50 mV (right). F_{gNa}=5.05. C: Delay between the onset of total I_{Na} in the two membranes as a function of cluster radius for different cleft widths (legend), for a V_{step} to –25 mV (left) and –50 mV (right). *Top*: For F_{gNa}=5.05. *Bottom*: For F_{gNa}=1.
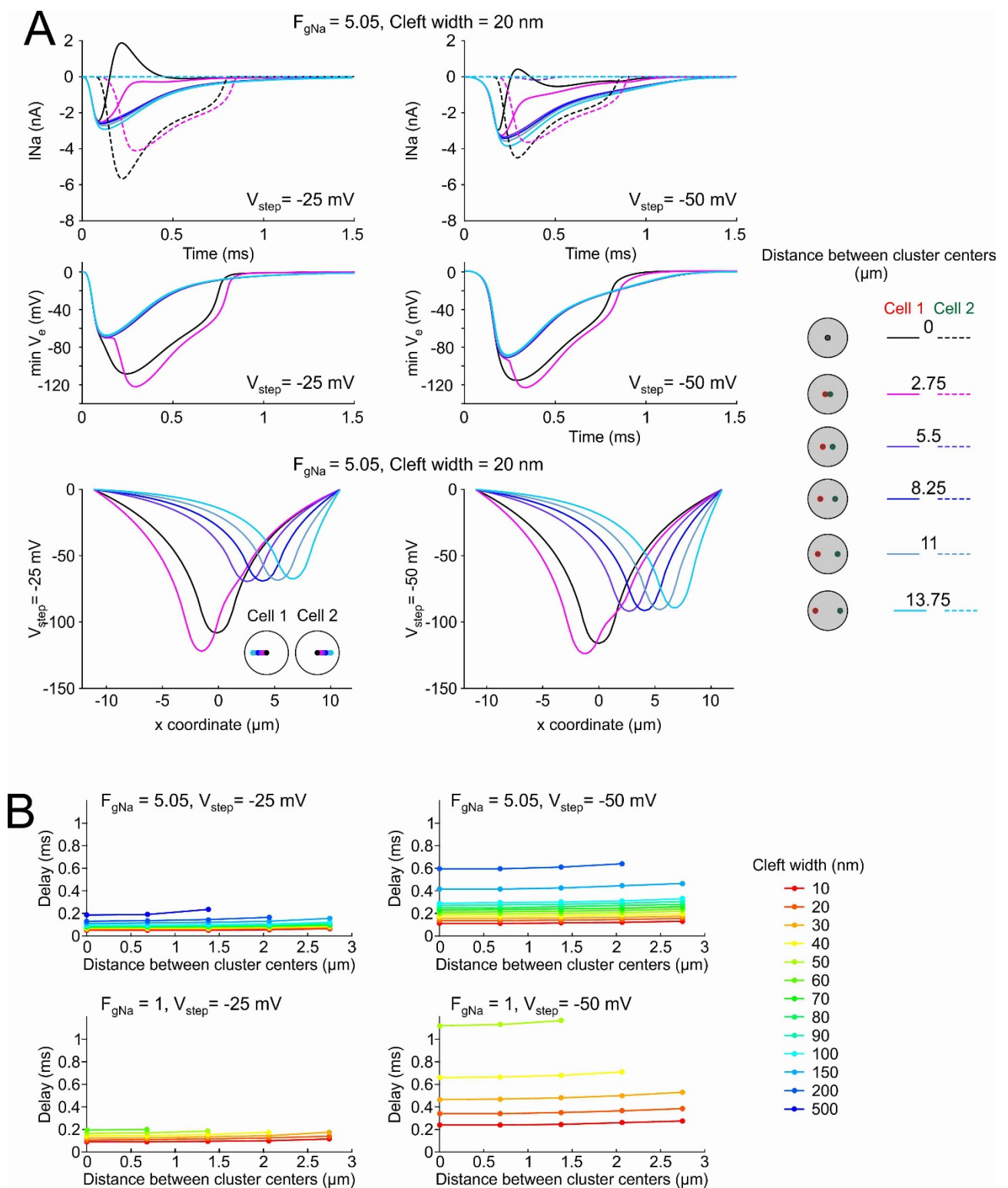
Figure 6. Effects of relative Na⁺ channel cluster position on I_{Na} and V_e in two membranes separated by a narrow cleft (R_{disc}=11 μm)

A: *Top*: Total I_{Na} in membrane 1 (full lines) and 2 (dashed lines) as a function of time for different relative positions of the clusters in the two membranes (see legend; cluster radii: 1.375 μm; F_{gNa}=5.05; cleft width: 20 nm), for a V_{step} to –25mV (left) and–50mV (right). *Middle*: Corresponding time courses of minimal V_e. *Bottom:* Corresponding spatial V_e profiles along the disc diameter at the time of occurrence of the minimal V_e. B: Delay between the onset of total I_{Na} in the two membranes as a function of the distance between the cluster centres, for different cleft widths (legend), for a V_{step} to –25 mV (left) and –50 mV (right). *Top*: For F_{gNa}=5.05. *Bottom*: For F_{gNa}=1.
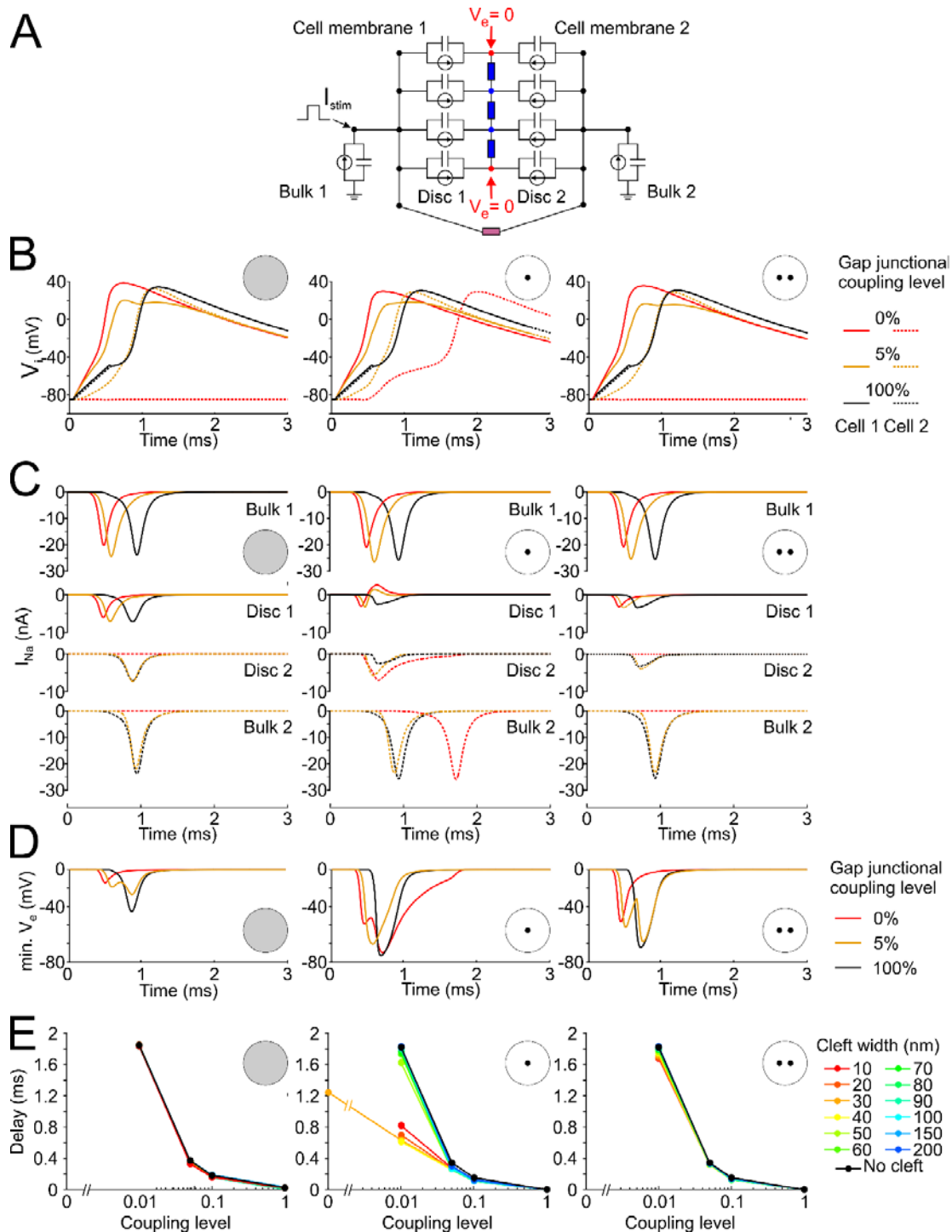
Figure 7. Interactions between ephaptic and gap junctional coupling between two cells
A: Schematic of the 2-cell model incorporating an intercalated disc (radius: 11 µm) and 2 disc membranes with membrane capacitance, ion currents and extracellular resistive properties (blue) and gap junctional resistance (pink). The discs were connected to elements representing the bulk membranes of the cells (100 µm long cylinders). The intracellular nodes were subjected to a current clamp protocol and the first cell was stimulated by a rectangular current pulse (duration: 0.5 ms; intensity: 11.5 nA). F_{gNa}=5.05. Cleft width: 30 nm. B: Intracellular potential as a function of time in cell 1 (full line) and cell 2 (dashed line) at different gap junctional coupling levels (100%, 5% and 0% of normal; legend). *Left:* Uniform Na^+ channel distribution in both intercalated disc membranes. *Middle:* Two aligned central Na^+ channel clusters ($R_{cluster}$=1.375 µm). *Right:* Two misaligned Na^+ channel clusters ($R_{cluster}$=1.375 µm; distance between centres: 2.75 µm). C: Corresponding I_{Na} through the bulk membrane of cell 1 (first row), the disc membrane of cell 1 (second row), the disc membrane of cell 2 (third row) and the bulk membrane of cell 2 (fourth row). D: Corresponding minimal V_e. E: Activation delay between the two cells as a function of gap junctional coupling level, for different cleft widths (legend) and for the three Na^+ channel distributions.

Movies

Movie 1

V_e, I_{Na} density, activation gate *m* and product of inactivation gates *hj* during a voltage step to –25 mV in the model of a disc-shaped membrane (radius: 11 µm) separated from a non-conducting obstacle by a 20 nm cleft (uniform distribution of g_{Na}, F_{gNa}=10.09).

Movie 2

V_e, I_{Na} density, activation gate *m* and product of inactivation gates *hj* during a voltage step to –50 mV in the model of a disc-shaped membrane (radius: 11 µm) separated from a non-conducting obstacle by a 20 nm cleft (uniform distribution of g_{Na}, F_{gNa}=10.09).

Movie 3

V_e, I_{Na} density, activation gate *m* and product of inactivation gates *hj* during a voltage step to –25 mV in the model of a disc-shaped membrane (R_{disc}: 11 µm) separated from a non-conducting obstacle by a 40 nm cleft and containing a centred cluster of Na^+ channels (F_{gNa}=5.05; $R_{cluster}$=0.125·R_{disc}).

Movie 4

V_e, I_{Na} density, activation gate *m* and product of inactivation gates *hj* during a voltage step to –50 mV in the model of a disc-shaped membrane (R_{disc}: 11 µm) separated from a non-conducting obstacle by a 40 nm cleft and containing a centred cluster of Na^+ channels (F_{gNa}=5.05; $R_{cluster}$=0.125·R_{disc}).

Movie 5

V_e, I_{Na} density in membrane 1 and 2 (I_{Na1} and I_{Na2}), corresponding activation gates m_1 and m_2 and products of inactivation gates h_1j_1 and h_2j_2 during a voltage step to –25 mV in the model of 2 disc-shaped membranes (R_{disc}: 11 µm) separated by a 20 nm cleft (F_{gNa}=5.05). Each membrane contains a cluster of Na^+ channels outlined in red for cell 1 and green for cell 2 ($R_{cluster}$: 1.375 µm) and the distance between cluster centres is 2.75 µm.

Movie 6

V_e, I_{Na} density in membrane 1 and 2 (I_{Na1} and I_{Na2}), corresponding activation gates m_1 and m_2 and products of inactivation gates h_1j_1 and h_2j_2 during a voltage step to –50 mV in the model of 2 disc-shaped membranes (R_{disc}: 11 µm) separated by a 20 nm cleft (F_{gNa}=5.05). Each membrane contains a cluster of Na^+ channels outlined in red for cell 1 and green for cell 2 ($R_{cluster}$: 1.375 µm) and the distance between cluster centres is 2.75 µm.

The movies can be viewed at [http://dx.doi.org/10.1113/JP275351].